Geochimica et Cosmochimica Acta 422 (2026) 258–270

Contents lists available at ScienceDirect

Geochimica et Cosmochimica Acta

journal homepage: www.elsevier.com/locate/gca

Sulfur contents in zircon-hosted and separated apatite in Archean TTGs: implications for the redox state of Archean felsic magmas☆

Jiazhen Wang [a,*], Ming Tang [a], Hao Chen [a], Xiao-Lei Wang [b], Bin Wu [c]

[a] SKLab-DeepMinE, MOEKLab-OBCE, School of Earth and Space Sciences, Peking University, Beijing 100871, China
[b] School of Earth Sciences and Engineering, Nanjing University, Nanjing 210023, China
[c] State Key Laboratory of Nuclear Resources and Environment, East China University of Technology, Nanchang 330013, China

ARTICLE INFO

Co-Guest Editor: Xiao-Ming Liu

Keywords:
Apatite
Sulfur
Archean TTG
Magmatic redox

ABSTRACT

Here we use sulfur-in-apatite to constrain the oxidation states of Archean TTGs (tonalite-trondhjemite-granodiorite) from the North China Craton, Kaapvaal Craton, and Pilbara Craton. We measured the sulfur contents of both zircon-hosted apatite and separated apatite in our TTG samples. We find that separated apatite tends to have lower sulfur contents in many samples. Besides, high sulfur contents are typically observed in the cores of apatite crystals. These observations together suggest that sulfur loss, likely due to metamorphism, fluid exsolution, or hydrothermal alteration, may have been pervasive during or after TTG formation. Therefore, zircon-hosted apatite is more likely to preserve primary magmatic sulfur signatures. Our results show that high apatite sulfur contents (>1000 ppm, up to ~3000 ppm) are present in TTGs from all three Archean cratons and samples as old as the Paleoarchean. Since high sulfur contents in apatite require the presence of sulfate in the melt, our findings point to widespread occurrence of oxidized TTG magmas in the Archean, with some samples showing oxygen fugacities >FMQ + 1.4, similar to the oxidized Phanerozoic arc magmas. The oxidation of the Archean TTG magmas was likely endogenic, through either garnet fractionation or kinetic water dissociation processes.

1. Introduction

Constraining the redox states of magmatic systems is important for understanding magmatic differentiation, mineralization, volatile composition of volcanism, and chemical weathering of the Earth's crust (Evans, 2012; Gaillard et al., 2011; Stüeken et al., 2012; Tomkins et al., 2012). Tonalite-trondhjemite-granodiorite (TTG) rocks are recognized as the major felsic component of Archean cratons, providing important information on the composition and formation processes of the early continental crust (Moyen and Martin, 2012). The Archean TTG rocks are typically characterized by high SiO_2, high Na_2O/K_2O, negative Ti-Nb-Ta anomalies, and many exhibit high La/Yb ratios. TTG magmas are primarily considered to be generated by partial melting of hydrous mafic rocks with the residual phase containing amphibole and/or garnet, or high-pressure fractional crystallization of hydrous mafic melts (Arth and Hanson, 1972; Beaudry et al., 2025; Jagoutz et al., 2013; Moyen and Martin, 2012; Moyen and Stevens, 2006). TTGs could be formed either at the base of thickened continental crust or within the subducted oceanic slabs (Ge et al., 2018; Hastie et al., 2016; Hernández-Uribe, 2024; Johnson et al., 2017; Palin et al., 2016).

Many Archean TTGs have undergone varying degrees of metamorphism (Moyen and Martin, 2012), which makes it more difficult to constrain the redox conditions of TTG magmas compared with Phanerozoic samples. But in recent years, the redox states of Archean TTG magmas have been increasingly studied as more redox proxies have become available. Prouteau and Scaillet (2012) conducted experiments investigating slab melting conditions and concluded that slab-derived TTG magmas in the Archean were relatively reduced and S-poor. This conclusion is inconsistent with several more recent studies that suggest oxidized compositions for many Archean TTGs (Ge et al., 2023; Meng et al., 2021; Meng et al., 2022; Tang et al., 2024a). Using the geochemical compositions of various minerals, Meng et al. (2021) found that the oxygen fugacity (fO_2) of the Neoarchean TTG magmas in the southern Abitibi Subprovince (Canada) could reach FMQ to FMQ + 1.5. Later, Meng et al. (2022) studied TTGs from southeastern Superior Province (Canada) using an oxybarometer based on S-in-apatite. By measuring S contents and relative abundances of S^{6+}, S^{4+}, and S^{2-} in zircon-hosted apatite inclusions from their TTG samples, they concluded

☆ This article is part of a special issue entitled: 'In honor of Bill McDonough' published in Geochimica et Cosmochimica Acta.

* Corresponding author.
E-mail address: vecwang@pku.edu.cn (J. Wang).

https://doi.org/10.1016/j.gca.2025.10.027
Received 1 January 2025; Accepted 21 October 2025
Available online 26 October 2025
0016-7037/© 2025 Elsevier Ltd. All rights are reserved, including those for text and data mining, AI training, and similar technologies.

that there were oxidized S-rich magmas present in the Neoarchean. Ge et al. (2023) combined two Ce-based oxybarometers (Loucks et al., 2020; Smythe and Brenan, 2016) to study zircon in Archean granitoids from several cratons. Their results showed that the fO_2 of many Archean granitoids were above FMQ, which is higher than that of the Archean upper mantle (FMQ to FMQ−1, as estimated by various methods including $Fe^{3+}/\Sigma Fe$ ratio, olivine-melt V partitioning, and V/Sc ratio (Aulbach and Stagno, 2016; Aulbach et al., 2019; Gao et al., 2022; Li and Lee, 2004; Nicklas et al., 2019)). More recently, Tang et al. (2024a) studied zircon in the Neoarchean TTGs from the North China Craton. They found that the medium- and high-pressure TTGs (based on the classification proposed by Moyen (2011)) have high zircon Eu/Eu*, which cannot be explained by merely suppressing plagioclase retention/fractionation and requires oxidized parental melts with high Eu^{3+}/Eu^{2+} for these Neoarchean TTGs (minimum fO_2 of NNO to NNO + 1).

The work by Meng et al. (2022) demonstrated that S-in-apatite could serve as a potentially important oxybarometer to constrain the oxidation states of Archean TTGs. Similar methods have also been used on TTGs by Moreira et al. (2023). Sulfur is an important multivalent element in magmatic systems. In silicate melts, S primarily exists as S^{6+} and S^{2-}, and the oxidation of S^{2-} to S^{6+} occurs over a narrow fO_2 interval of 1–2 log units (Jugo, 2009; Wilke et al., 2008). Apatite is a widespread accessory mineral in various magmatic systems (Hughes and Rakovan, 2015). Sulfur in different valence states can enter the lattice of apatite through different incorporation mechanisms, but the ability of S^{6+} to be incorporated into apatite is significantly stronger than that of S^{2-} (Konecke et al., 2019, 2017b). As the fO_2 rises, the system becomes S^{6+}-dominated, and the bulk partition coefficient of S between apatite and silicate melt increases dramatically, leading to higher S content in apatite (Konecke et al., 2019, 2017b; Parat et al., 2011). Therefore, the drastically different partitioning behaviors of S^{6+} and S^{2-} in apatite make apatite S content a sensitive indicator of S valence and fO_2 of magmas (Konecke et al., 2019).

When applying the S-in-apatite oxybarometer to natural samples, one critical question is whether apatite can retain the primary magmatic S signatures, particularly for samples that experienced intense metamorphism or prolonged cooling and re-equilibration (e.g., many Archean TTGs). Previous studies mostly focused on apatite inclusions in zircon (e.g., Meng et al., 2022; Moreira et al., 2023), which were thought to better preserve primary magmatic S due to the resilience of zircon to metamorphism and weathering and the slow diffusivities for most elements in the zircon lattice (Cherniak and Watson, 2003). But many Archean TTG samples have very limited zircon-hosted apatite inclusions, resulting in insufficient data for studying the redox states of primary magmas. To provide insights into this problem, we compare data of separated apatite, which has larger sample sizes, with data of zircon-hosted apatite inclusions, which may be more reliable. Here, we carried out comprehensive measurements of S contents in apatite grains in TTG samples from three widely studied Archean cratons: the North China Craton, Kaapvaal Craton, and Pilbara Craton. In particular, we compared the S contents in separated apatite grains with those hosted in zircon. We also measured S contents in apatite on thin sections from the Kaapvaal Craton, along with the corresponding separated apatite and zircon inclusion data. We then used these new S-in-apatite data to constrain the S valence and fO_2 of Archean TTG melts.

2. Geological backgrounds and samples

The North China Craton is one of the oldest cratons in the world and preserves rock records as old as 3.8 Ga (Liu et al., 1992; Song et al., 1996). It consists of Archean to Paleoproterozoic basement that can be divided into two distinct blocks: the Eastern Block and the Western Block, and the intervening Trans-North China Orogen (Fig. 1A) (Zhao et al., 2005; Zhao and Zhai, 2013). Archean TTG gneisses form a major component of the Archean basement, with widespread and continuous TTG magmatism occurring from ~3.0 to 2.5 Ga (Wan et al., 2023). Approximately 80 % of the Archean basement is composed of 2.6 to 2.5 Ga TTG gneisses, along with associated ultramafic to mafic igneous rocks, charnockites, granites, and minor other lithologies (Zhao and Zhai, 2013).

The Kaapvaal Craton, centered in northeastern South Africa, is one of the oldest Archean cratons, formed through a complex interplay of tectonic processes and magmatism between ~3.6 and ~2.5 Ga (Poujol et al., 2003). The Barberton Granitoid-Greenstone Terrain (BGGT) lies on the eastern edge of the Kaapvaal Craton and is a well-preserved pre-3.0 Ga granitoid-greenstone terrane that contains both deformed TTG gneisses and relatively undeformed TTG units intruding into surrounding greenstones of the Barberton Greenstone Belt (BGB) (Fig. 1B) (Anhaeusser and Robb, 1980; Moyen et al., 2019). The BGB is surrounded by TTG rocks of varying ages, many of which are older than 3.2 Ga (Moyen et al., 2019).

The Pilbara Craton is one of only two pristine Archean 3.8–2.7 Ga cratons identified on Earth, and is located in the northwestern part of Western Australia (Hickman and Van Kranendonk, 2012). It consists of two major components: a Paleo- to Neoarchean basement composed of granites and greenstones, and overlying Neoarchean to Proterozoic volcano-sedimentary rocks forming the Fortescue and Hamersley basins (Fig. 1C) (Van Kranendonk et al., 2002). The North Pilbara terrain is mainly composed of three separated granite-greenstone terranes: the East Pilbara granite-greenstone terrane (3.7–2.8 Ga), the West Pilbara granite-greenstone terrane (3.3–2.9 Ga), and the Kuranna terrane (3.3–3.2 Ga). These terranes were separated by two major sedimentary basins: the Mallina basin (3.0–2.9 Ga), composed of volcanic and sedimentary rocks with associated granitoid rocks, and the Mosquito Creek basin, consisting of clastic rocks that were deformed into a fold and thrust belt at 2.9 Ga. (Van Kranendonk et al., 2002).

A total of 18 TTG samples were collected to determine the S contents in apatite, including five samples from the Eastern Block of the North China Craton, ten samples from the BGGT of the Kaapvaal Craton, and three samples from the Archean granite basement of the Pilbara Craton. The North China TTGs were collected from Qianxi (Hebei Province) and Tai'an (Shandong Province), both of which have outcrops of Archean TTG basement that formed in the Neoarchean (Fig. 1A). Samples MT21-3–6, MT21-4–10, and MT21-4–11 have been documented in Tang et al. (2024a), while MT21-3-9 and MT21-4-9 are newly reported in this study. These five samples include two tonalite (MT21-3-6, MT21-3-9) and three trondhjemite (MT21-4-9, MT21-4-10, MT21-4-11) (Fig. S1 in Supplementary Material). The Kaapvaal TTGs were collected from different plutons of the BGGT, including the Badplaas, Theespruit, Uitgevonden, Rooihoogte Pass, Kaap Valley, and Nederland pluton (Fig. 1B). All Kaapvaal samples have been documented in Wang et al. (2022). Most of them are classified as trondhjemite, with only one (14SA-23) plotting in the tonalite regime (Fig. S1). The three Pilbara TTG samples were all newly obtained core samples from the Geological Survey of Western Australia. WRL-31 was taken from 1916.78–1916.98 m of drill hole DD86WRL1, FVG-1 was from 1882.19–1882.39 m of DDH83FVG1, and SGS-4 was from 2777.37–2777.57 m of DD85SGS1. All three drill holes are located in the Hamersley basin (Fig. 1C), which is dominated by the volcano-sedimentary sequences of the Mt Bruce Supergroup deposited between ~2.8 and ~2.4 Ga (Arndt et al., 1991). These sequences overlie older Archean TTG basement rocks, which are the source of our samples. WRL-31 is classified as granodiorite, while FVG-1 and SGS-4 are trondhjemites (Fig. S1).

The thin section photomicrographs of our samples show typical TTG characteristics with evident metamorphic overprinting (Fig. S2). The mineral assemblage is primarily composed of plagioclase, quartz, alkali feldspar, hornblende, and biotite, with accessory minerals such as zircon, apatite, sphene, epidote, and chlorite. In many samples, perthitic and myrmekitic exsolution textures in feldspar can be observed. Nearly all samples display varying degrees of sericitization of plagioclase and chloritization of biotite. In some Kaapvaal samples, clear directional stretching of minerals like quartz and biotite can be observed, indicating

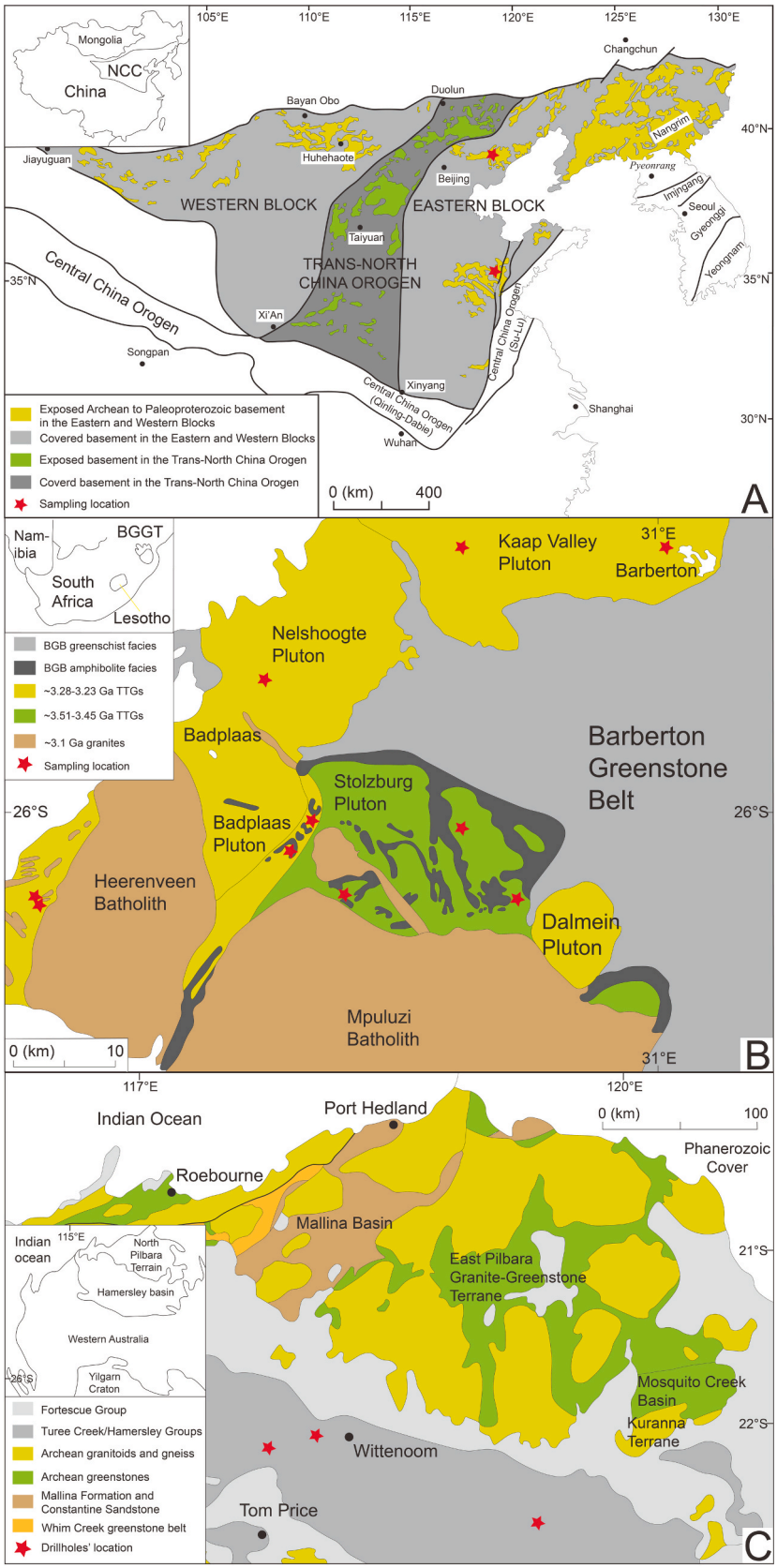


Fig. 1. Simplified geologic maps of (A) the North China Craton (modified from Zhao et al. (2005)); (B) the BGGT to the east and northeast of Badplaas (modified from Wang et al. (2022)); (C) the North Pilbara terrain (modified from Van Kranendonk et al. (2002)).

intense stress conditions. The Pilbara samples show more intense metamorphism, with pervasive cracks filled by high-interference color hydrothermal minerals observed throughout the thin sections. Apatite in the thin sections usually exhibit euhedral to subhedral hexagonal prismatic or needle-like crystals (10–100 μm). Under crossed polarizers, apatite displays first-order gray-white interference colors with parallel extinction. Many grains are partially or fully encapsulated by plagioclase, hornblende, or biotite. No significant corrosion or alteration textures are observed.

3. Analytical methods

For our newly collected TTG samples, we first crushed the rocks, picked out zircon and apatite grains, and then mounted them in epoxy respectively. Separated apatite grains are typically >100 μm in diameter, while zircon-hosted apatite inclusions are very small with diameters of 5–10 μm. The thin sections were obtained by cutting and polishing the rocks directly. The thin section apatite mentioned in this article refers to the apatite grains identified on thin sections. These apatite grains vary in size (10–100 μm), and some small grains are encapsulated by other minerals such as plagioclase and biotite.

For whole-rock powders, the major element analysis was conducted on an X-ray fluorescence spectrometer (XRF), and trace elements were analyzed on an inductively coupled plasma-mass spectrometer (ICP-MS). Zircon mounts were analyzed for U-Pb dating on a laser ablation-inductively coupled plasma-mass spectrometer (LA-ICP-MS). Cathodoluminescence (CL) images of separated apatite on apatite mounts were generated by a field emission-scanning electron microscope (FE-SEM). For separated apatite grains on apatite mounts, zircon-hosted apatite inclusions on zircon mounts, and apatite grains on thin sections, we measured elemental abundances using an electron probe micro analyzer (EPMA). For selected apatite grains with high S contents, we carried out EPMA mapping of S distributions. Detailed analytical methods are reported in Supplementary Material.

4. Results

4.1. Zircon U-Pb dating and whole-rock compositions

Our North China samples have SiO_2 contents of 63–73 wt% (Table 1). Their zircon U-Pb dating results show that these TTGs range from 2645 to 2546 Ma in age. The samples have typical geochemical features of TTGs, such as low K_2O/Na_2O ratios (0.1–0.5), high Sr/Y (98–268, average = 163), and high La/Yb (24–53, average = 40). The Kaapvaal samples have SiO_2 contents of 61–71 wt%, and their zircon U-Pb dating yields ages of 3453 to 3107 Ma. These TTGs also have low K_2O/Na_2O ratios (0.1–0.3), high Sr/Y (30–239, average = 97), and high La/Yb (16–97, average = 45). Three Pilbara samples have SiO_2 contents of 70–71 wt%, and zircon U-Pb dating shows ages of 3119 to 3015 Ma. The K_2O/Na_2O ratios of Pilbara samples are relatively high (0.5–0.9), and Sr/Y ratios are relatively low (8–48, average = 23) compared with North China samples and Kaapvaal samples. Their La/Yb ratios are at the same

Table 1
Sample ages and element compositions.

Sample	Craton	Rock type	Age, Ma (±2 se)	SiO_2	TiO_2	Al_2O_3	FeO_T	MnO	MgO	CaO	Na_2O	K_2O	P_2O_5	LOI	K_2O/Na_2O	Sr/Y	La/Yb
MT21-3-6*	North China Craton	Tonalite	2547 ± 8	68.80	0.38	15.16	3.48	0.04	1.69	3.76	4.68	1.07	0.11	0.80	0.2	98	36
MT21-3-9	North China Craton	Tonalite	2546 ± 7	63.20	0.59	16.98	4.97	0.07	2.38	5.33	5.04	0.52	0.17	0.63	0.1	132	24
MT21-4-9	North China Craton	Trondhjemite	2645 ± 5	72.50	0.17	15.34	1.15	0.02	0.41	1.81	5.15	2.64	0.06	0.56	0.5	176	53
MT21-4-10*	North China Craton	Trondhjemite	2599 ± 27	71.40	0.22	15.81	1.43	0.03	0.56	2.23	5.47	2.26	0.08	0.50	0.4	141	39
MT21-4-11*	North China Craton	Trondhjemite	2598 ± 25	72.19	0.18	15.43	1.16	0.02	0.42	1.98	5.11	2.64	0.06	0.57	0.5	268	48
14SA-16**	Kaapvaal Craton	Trondhjemite	3232 ± 4	71.07	0.32	16.25	2.02	0.02	0.92	3.00	5.07	1.41	0.09	0.39	0.3	143	38
14SA-18-1**	Kaapvaal Craton	Trondhjemite	3266 ± 6	70.85	0.09	18.32	0.01	0.00	0.17	4.01	6.05	0.35	0.03	0.40	0.1	239	97
14SA-22**	Kaapvaal Craton	Trondhjemite	3453 ± 3	68.76	0.29	15.90	2.19	0.04	1.12	2.52	5.32	1.79	0.07	1.20	0.3	53	17
14SA-23**	Kaapvaal Craton	Tonalite	3222 ± 4	61.04	0.52	16.49	4.97	0.07	2.78	4.24	4.94	1.35	0.22	3.01	0.3	44	24
14SA-25**	Kaapvaal Craton	Trondhjemite	3226 ± 7	66.01	0.40	15.81	3.80	0.04	1.58	2.43	5.24	1.03	0.14	2.75	0.2	82	16
16SA-1**	Kaapvaal Craton	Trondhjemite	3107 ± 5	71.07	0.32	16.25	2.02	0.02	0.92	3.00	5.07	1.41	0.09	0.39	0.3	30	44
16SA-9-2**	Kaapvaal Craton	Trondhjemite	3230 ± 11	64.42	0.63	16.88	3.64	0.05	1.34	3.42	5.39	1.87	0.24	1.09	0.3	92	82
16SA-28-1**	Kaapvaal Craton	Trondhjemite	3250 ± 6	71.19	0.32	15.97	2.04	0.03	0.81	2.96	5.03	1.09	0.10	0.40	0.2	127	37
16SA-29**	Kaapvaal Craton	Trondhjemite	3244 ± 5	68.40	0.41	16.98	2.35	0.04	1.07	3.61	5.11	1.13	0.13	0.39	0.2	94	44
16SA-34**	Kaapvaal Craton	Trondhjemite	3232 ± 12	70.19	0.17	16.29	1.38	0.04	0.90	2.02	6.11	1.83	0.06	0.58	0.3	68	55
WRL-31	Pilbara Craton	Granodiorite	3032 ± 30	70.57	0.21	14.81	1.73	0.07	0.65	2.13	3.15	2.88	0.07	3.32	0.9	8	21
FVG-1	Pilbara Craton	Trondhjemite	3015 ± 55	70.98	0.32	14.40	2.37	0.03	0.70	1.47	4.28	3.20	0.14	1.53	0.7	48	82
SGS-4	Pilbara Craton	Trondhjemite	3119 ± 13	69.82	0.43	14.71	3.05	0.05	1.16	2.49	4.48	2.12	0.17	1.44	0.5	11	10

Notes:
*Whole-rock data from Tang et al. (2024a).
**Whole-rock data from Wang et al. (2022).

level as other samples (10–82, average = 38). The detailed whole-rock major and trace element and the zircon geochronology data are reported in Supplementary Material.

4.2. Apatite cathodoluminescence imaging

Our separated apatite CL imaging shows diverse patterns (Fig. S5). Most apatite grains display irregular, heterogeneous distributions of brightness and darkness. Some grains exhibit dark cores with bright rims, while many grains with cracks show bright bands along the cracks. A few grains appear completely dark. In some samples, the apatite displays oscillatory zoning similar to zircon CL images.

4.3. Sulfur contents in apatite

For the 18 TTG samples from the three cratons, we measured both separated apatite and zircon-hosted apatite inclusions. For seven samples (14SA-18–1, 14SA-22, 14SA-23, 14SA-25, 16SA-1, 16SA-9–2, 16SA-29) from the Kaapvaal Craton, we also measured apatite in situ on thin sections (data are reported in Supplementary Material). After removing invalid data below the detection limit of S (<45 ppm, see caption of Fig. 2 for the detailed proportions of these low-S apatite analyses), we obtained data for 98 separated apatite grains and 62 zircon-hosted apatite inclusions for the North China TTG samples, 191 separated apatite grains, 88 zircon-hosted apatite inclusions, and 91 thin section apatite grains for the Kaapvaal TTG samples, and 74 separated apatite grains and 43 zircon-hosted apatite inclusions for the Pilbara TTG samples.

Fig. 2 shows the S content distributions for both separated apatite and zircon-hosted apatite inclusions in the 18 TTG samples we measured. For nearly all samples, the S contents in zircon-hosted apatite are higher than or similar to those in separated apatite. The S contents in separated apatite from the North China TTGs mainly range from 200 to 500 ppm with no data exceeding 1000 ppm, whereas zircon-hosted apatite exhibit overall higher S contents, including data above 1000 ppm (Figs. 2A, D). The S contents in nearly all separated apatite from the Kaapvaal TTGs are below 500 ppm. Although most zircon-hosted apatite inclusions also record low S contents (<500 ppm), high S contents (>1000 ppm) are still observed in many samples (Figs. 2B, E). The apatite in the Pilbara TTGs have the highest S contents among the three cratons, with the average S contents in both separated apatite and zircon-hosted apatite generally exceeding 1000 ppm (Figs. 2C, F).

Fig. 3A shows the average S contents in separated apatite and zircon-hosted apatite for each sample, which again suggests that zircon-hosted apatite tends to have higher S contents than separated apatite. Fig. 3B is the cumulative distributions of S contents in separated apatite, zircon-hosted apatite, and thin section apatite for seven selected Kaapvaal samples (14SA-18-1, 14SA-22, 14SA-23, 14SA-25, 16SA-1, 16SA-9-2, 16SA-29). The S content distribution of thin section apatite lies between zircon-hosted apatite and separated apatite.

Fig. 4 illustrates the relationships between S contents in apatite and ages, whole-rock K_2O/Na_2O, and Ba/Th ratio. Archean TTGs with S-in-apatite above 1000 ppm are present in all three cratons studied here, and the oldest TTGs with high apatite S contents occur at ~3230 Ma (Fig. 4A). There is no clear temporal trend in apatite S content in our samples. Sample average S contents in zircon-hosted apatite also do not show correlations with whole-rock K_2O/Na_2O and Ba/Th, two key proxies that serve as indicators for magma affinity and slab-derived fluid input, respectively (Figs. 4B, C).

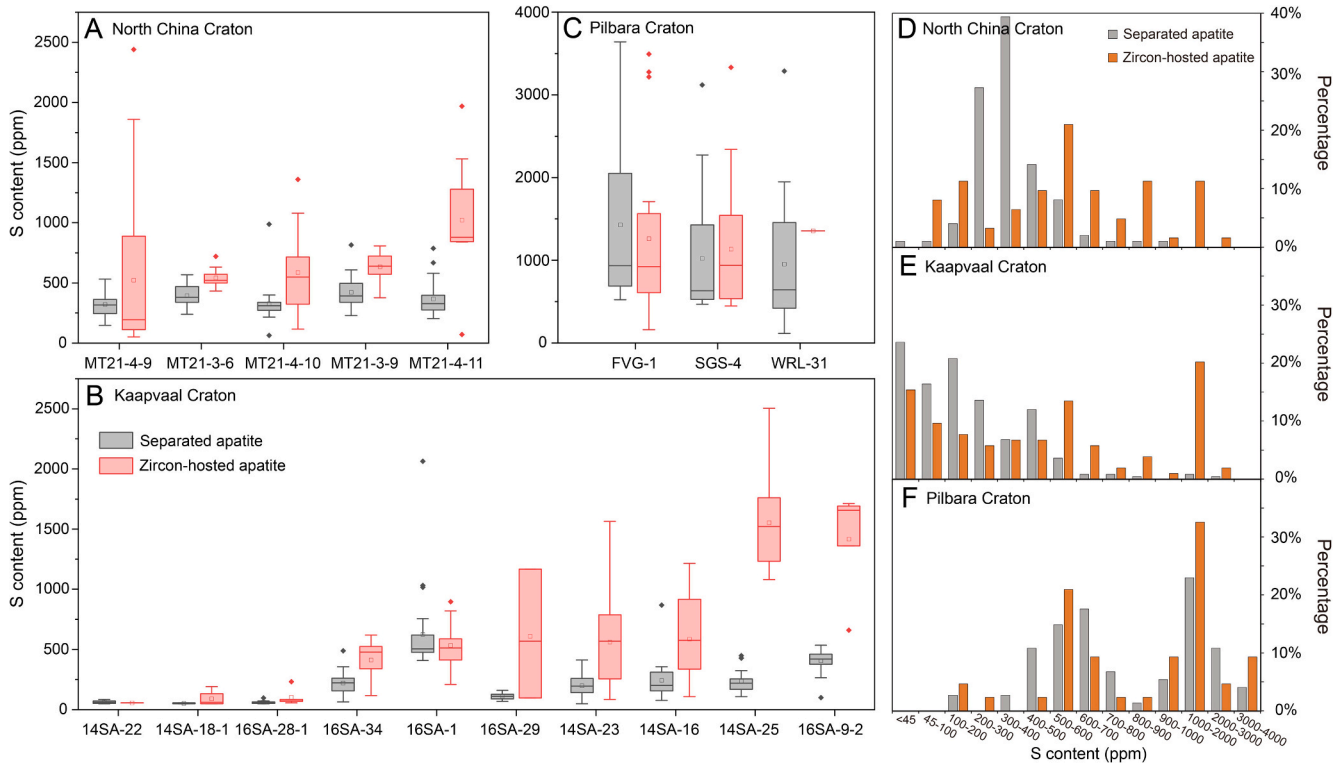


Fig. 2. Boxplots of S contents in apatite in each TTG sample (A, B, C) and apatite S content distribution (D, E, F). (A) The North China TTGs; (B) the Kaapvaal TTGs; (C) the Pilbara TTGs. The hollow squares represent the average values. The rectangular box extends from the lower quartile to the upper quartile, with an internal line marking the median. Upper/lower whiskers indicate non-outlier data range, while diamond symbols represent outliers beyond 1.5 times the interquartile range. (D) The five North China TTGs with a total of 99 separated apatite (including one data lower than the detection limit) and 62 zircon-hosted apatite inclusions. (E) The ten Kaapvaal TTGs with a total of 250 separated apatite (including 59 data lower than the detection limit) and 104 zircon-hosted apatite inclusions (including 16 data lower than the detection limit). (F) The three Pilbara TTGs with a total of 74 separated apatite and 43 zircon-hosted apatite inclusions.

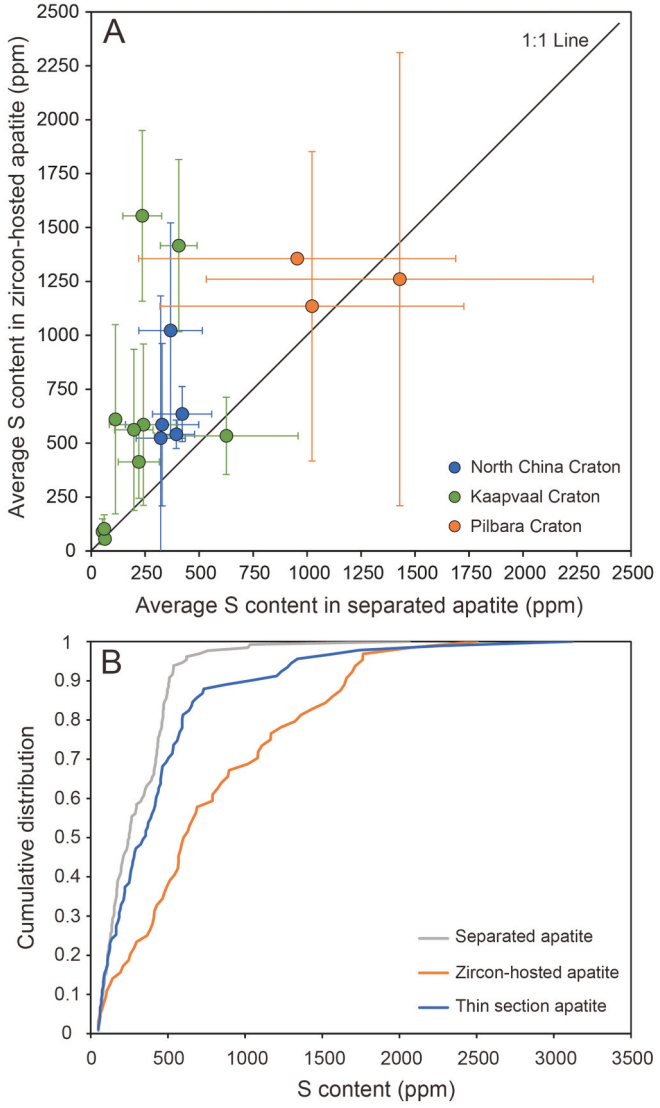


Fig. 3. Comparison of S contents in separated apatite, zircon-hosted apatite, and thin section apatite. (A) The average values of S contents in separated apatite and zircon-hosted apatite for each sample. Error bars represent ± 1 standard deviation. (B) The cumulative distribution of S contents in three types of apatite from seven selected Kaapvaal TTGs.

4.4. EPMA mapping

We mapped 52 apatite grains (including separated, zircon-hosted, and thin section apatite) with S contents ranging from a few hundred to several thousand ppm (Figs. 5, 6, and Figs. S6–S11). While most low-S grains (<1000 ppm) are homogeneous in S distributions, many grains show S enrichments in the cores. For separated apatite from the North China and Kaapvaal samples, most grains show homogeneous S distributions, only a few showing slight S enrichments in the cores. As for separated apatite from the Pilbara samples, all grains exhibit a distinctive distribution pattern: S is enriched in the cores and has low content at the rims, with sharp and distinct boundaries between (Fig. 5D and Fig. S8). For zircon-hosted apatite inclusions, some also show signs of S enrichments in the cores, but the distributions are hard to resolve by EPMA mapping due to the small sizes of most inclusions (<10 μm) and the edge effect (signal inaccuracies caused by geometric and physical variations at mineral boundaries during electron probe analysis) (Fig. 6 and Figs. S9, S10).

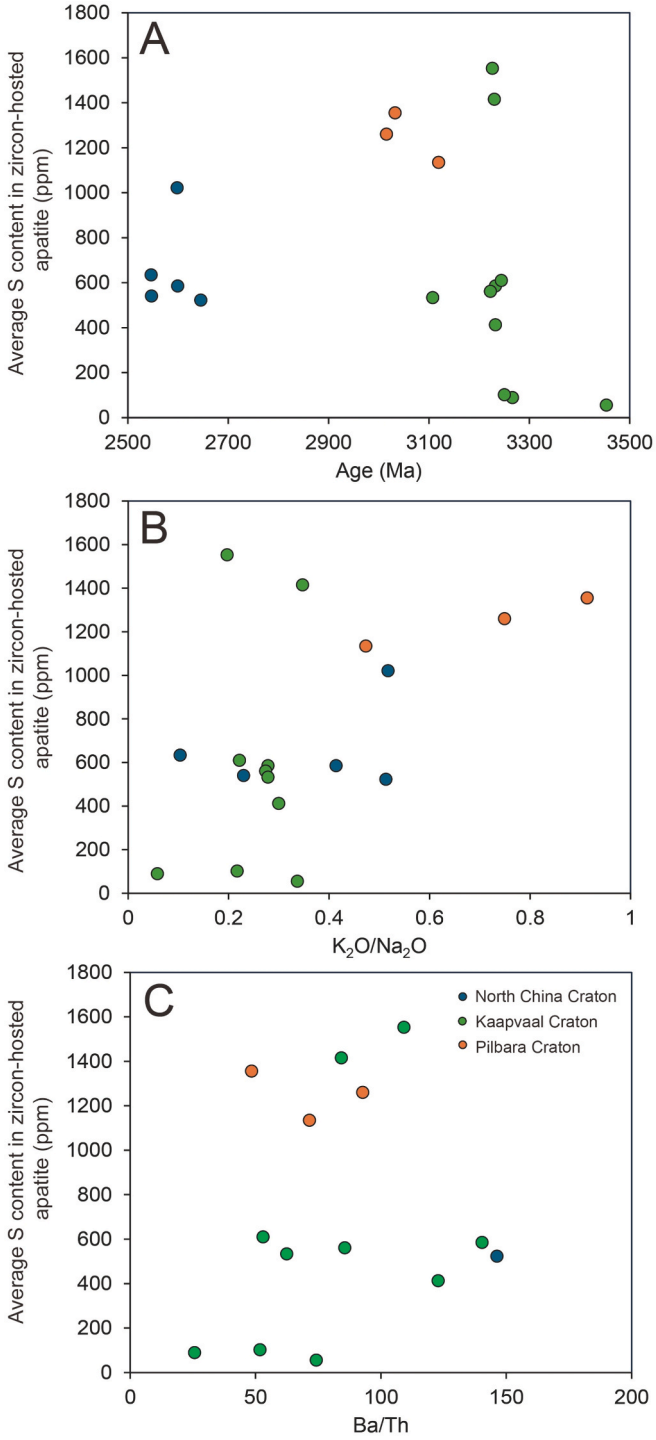


Fig. 4. Relationships between S contents in apatite and ages, whole-rock K_2O/Na_2O, and Ba/Th ratio. (A) Sample average S content in zircon-hosted apatite versus TTG zircon U-Pb age. (B) Sample average S content in zircon-hosted apatite versus whole-rock K_2O/Na_2O. (C) Sample average S content in zircon-hosted apatite versus whole-rock Ba/Th.

5. Discussion

5.1. Sulfur loss in separated apatite

Metasomatism, re-equilibrium, or recrystallization during interaction with S-rich oxidized (high $S^{6+}/\Sigma S$) hydrothermal fluids can lead to an increase in S content in apatite (Harlov et al., 2025; Konecke et al.,

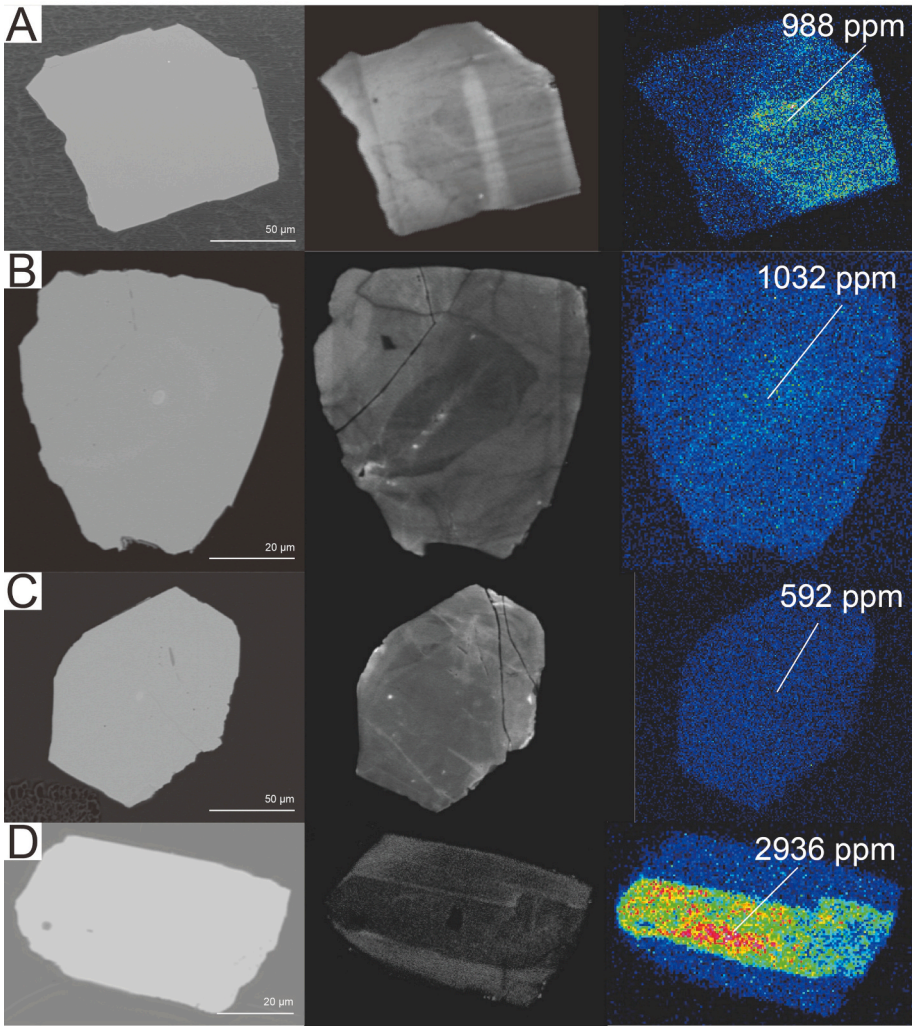


Fig. 5. Backscattered electron imaging (left), cathodoluminescence imaging (middle), and sulfur mapping (right) of selected separated apatite grains. For mapping results, brighter colors indicate higher S contents (e.g., orange to red), while darker colors indicate lower S contents (e.g., blue to black). (A) MT21-4-10_2 from the North China Craton; (B) 16SA-1_4 from the Kaapvaal Craton; (C) 16SA-1_5 from the Kaapvaal Craton; (D) FVG-1_3 from the Pilbara Craton.

2017a; Sadove et al., 2019). These processes are more likely to alter S-in-apatite in separated apatite grains than in zircon-hosted apatite inclusions because separated apatite grains predominantly consist of unprotected grains lacking mineral encapsulation. However, none of our samples show significantly higher S contents in separated apatite than those of zircon-hosted apatite, even for those samples with extremely low apatite S contents (<100 ppm, e.g., 14SA-22, 14SA-18-1, and 16SA-28-1). Rather, the higher S contents recorded by zircon-hosted apatite inclusions point to predominant S loss during late-stage differentiation or post-crystallization processes, such as S outward diffusion, or re-equilibrium with late-stage low $S^{6+}/\Sigma S$ fluids/melts, or apatite crystallization after S degassing.

Our thin section apatite data further support S loss in separated apatite (Fig. 3B). The thin section apatite grains are intermediate in size between the zircon-hosted apatite inclusions and separated apatite grains. Notably, some of the measured apatite grains on thin sections, particularly those small ones with ~10 μm in diameter, are partially or fully encapsulated by minerals such as biotite and plagioclase (Fig. S11). Although these host minerals are less resistant to alteration than zircon and have higher diffusivities for most elements than zircon (Cherniak and Watson, 2003 and references therein), they still provide partial protection against hydrothermal and/or metamorphic resetting. This may explain why the S content distribution of thin section apatite plots between zircon-hosted apatite inclusions and separated apatite grains, most of which existed in the matrix and were thus least protected.

The combination of apatite EPMA mapping results and CL images provides additional insights into the late-stage re-equilibrium and/or alterations that separated apatite may have undergone. The CL images of separated apatite exhibit complex patterns (Fig. S5, the brightness and darkness of apatite CL images are generally considered to be related to REE (rare earth element) content, with brighter areas corresponding to higher REE concentrations (Xing and Wang, 2017)). These complex patterns, along with the petrographic observations (e.g., extensive sericitization of plagioclase, distinct hydrothermal cracks and associated hydrothermal mineral growth within) of the samples, indicate that these samples experienced hydrothermal alteration (Xing and Wang, 2017). However, for most separated apatite grains, their CL patterns do not correlate with EPMA mapping results. Even in cases where bright cracks (indicating REE-rich hydrothermal alteration along cracks) are visible in CL images, S distributions do not follow these alteration cracks. Therefore, S leaching through hydrothermal alteration along mineral cracks may be limited and is unlikely to be the primary cause of S loss in separated apatite.

It is also interesting to note that some separated apatite grains show S zoning, and in these grains, the cores almost always show higher S contents than the rims (Fig. 5 and Figs. S6, S7). This rimward depletion of S content provides further evidence for S loss, likely due to long-term outward diffusion. For separated apatite grains in Pilbara TTGs, their

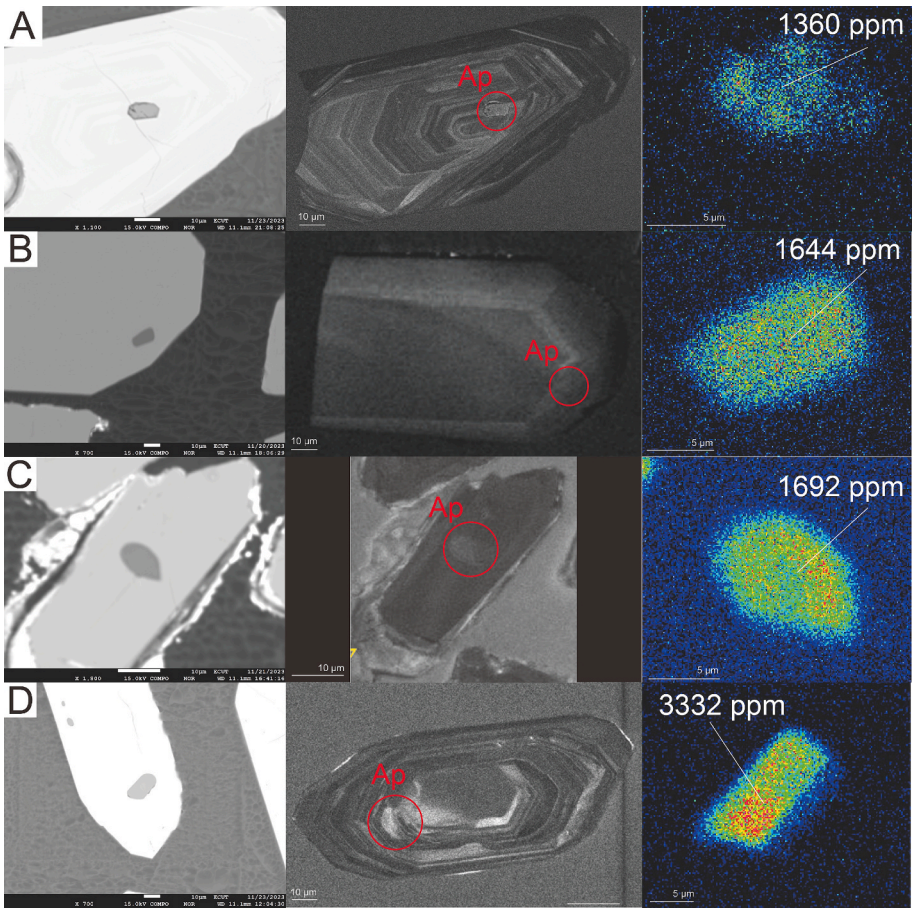


Fig. 6. Backscattered electron imaging (left), cathodoluminescence imaging (middle), and sulfur mapping (right) of selected zircon-hosted apatite inclusions. For mapping results, brighter colors indicate higher S contents (e.g., orange to red), while darker colors indicate lower S contents (e.g., blue to black). (A) MT21-4-10_in_5 from the North China Craton; (B) 14SA-25_in_8 from the Kaapvaal Craton; (C) 16SA-9-2_in_5 from the Kaapvaal Craton; (D) SGS-4_in_25 from the Pilbara Craton.

EPMA mapping results show a pattern where S is enriched in the cores and depleted at the rims, with sharp and distinct boundaries between (Fig. 5D, Fig. S8). Their CL images exhibit a similar pattern, whereas the S-rich cores appear darker, and the S-poor rims appear brighter. Compared with the S-rich cores, which may have crystallized from felsic melts with regular REE contents, the S-poor rims likely formed through recrystallization in REE-rich hydrothermal fluids/melts. Our mapping results also show that the S contents of zircon are extremely low, and even cracks near apatite do not show any correlation with S (Fig. 6, Figs. S9, S10), further supporting the reliability of the inclusion data. Overall, we suggest that S loss may have been ubiquitous in separated apatite grains in TTGs, and zircon-hosted apatite inclusion data provide a more reliable record for studying S contents and oxidation states in TTGs.

5.2. The redox states of Archean felsic magmas

Here we use the data of S contents in zircon-hosted apatite to constrain the redox states of Archean TTG magmas. We adopt the approach of Tang et al. (2020a) and calculate the minimum $S^{6+}/\Sigma S$ and fO_2 of the TTG melts. Sulfur content at sulfide saturation (SCSS) provides an estimate of the maximum S^{2-} content in silicate melts. Under conditions where fO_2 lies below the S^{2-} to S^{6+} transition, SCSS typically correlates positively with melt FeO_T content, temperature, H_2O content, and negatively with SiO_2 content (Baker and Moretti, 2011; Fortin et al., 2015; Jego and Dasgupta, 2014; Liu et al., 2007; Smythe et al., 2017). For both H_2O saturated and undersaturated rhyolitic melts at 800 °C and 500 MPa, SCSS is very low, rarely exceeding 100 ppm (Baker and Moretti, 2011). Because S^{2-} is incompatible with apatite (Konecke et al., 2019, 2017b), we assume that S^{2-} has a maximum partition coefficient of 1 between apatite and melt. This assumption leads to a maximum S^{2-} content in apatite of ~100 ppm. This would mean that a total S content above ~100 ppm in apatite is due to the presence of S^{6+}. For S^{6+} partitioning in apatite, Parat et al. (2011) established an empirical relationship between S contents in apatite and melt based on crystallization experiments and natural sample data under oxidized conditions. Their experiments covered various P-T conditions in intermediate, felsic, and carbonatitic rocks. With these results, we first calculate the minimum S^{6+} in apatite by subtracting the maximum S^{2-} in apatite (approximated by SCSS) from the total S content in apatite measured by EPMA. Then, we use the empirical relationship for S^{6+} partitioning between apatite and melt from Parat et al. (2011) to calculate the S^{6+} content and $S^{6+}/\Sigma S$ in the TTG melt.

Our analyzed zircon-hosted apatite inclusions record S contents up to ~3500 ppm. Over 30 % of all the analyzed apatite inclusions show S contents >1000 ppm, and apatite inclusions with >2000 ppm S are seen in TTG samples from all three cratons (Fig. 2). These high apatite S contents indicate that there are TTGs from each craton having melt $S^{6+}/\Sigma S$ of 0.61 and fO_2 of >FMQ + 1.4. In particular, the TTGs from the Pilbara Craton may have had melt $S^{6+}/\Sigma S$ and fO_2 of up to 0.94 and >FMQ + 1.9, respectively (Fig. 7).

5.3. Widespread sulfate-containing felsic magmatism in the Archean?

Our observations of high-S apatite in TTGs from the North China Craton, Kaapvaal Craton, and Pilbara Craton, together with the similar

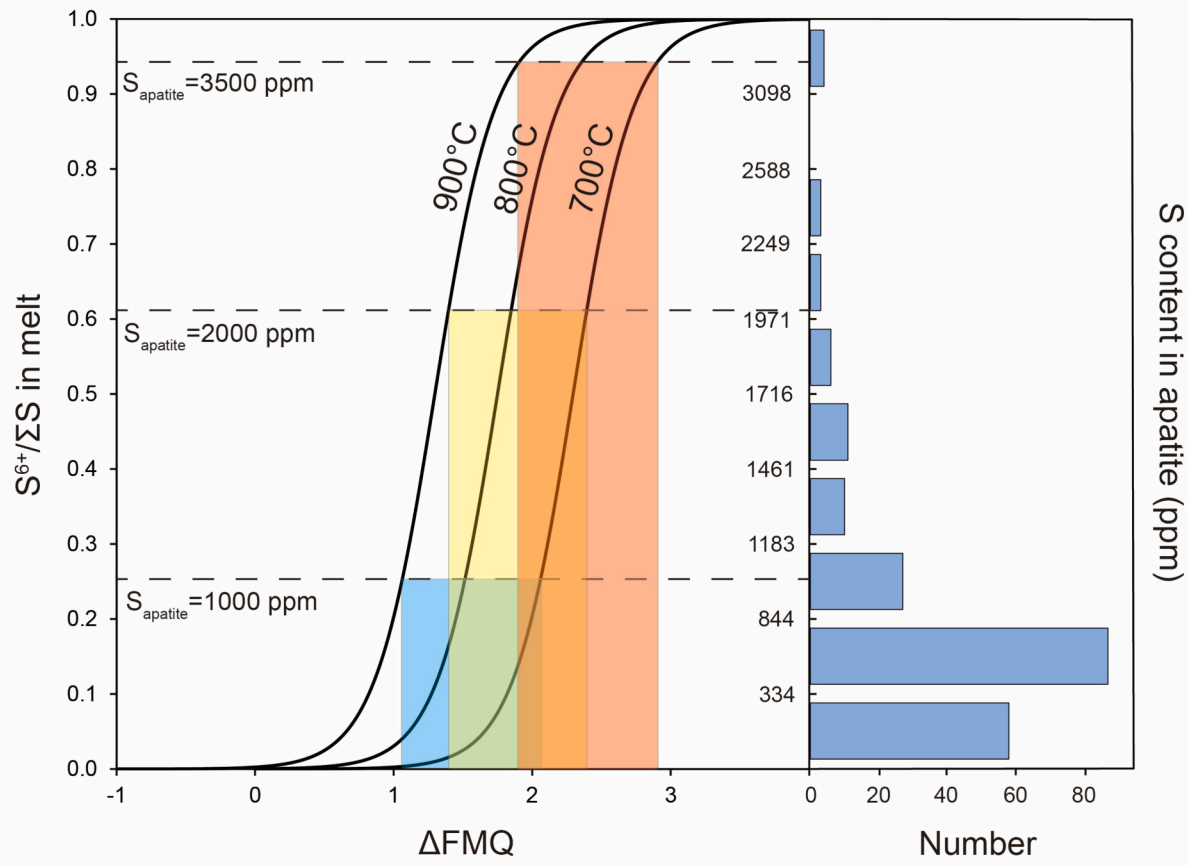


Fig. 7. The minimum $S^{6+}/\Sigma S$ and the corresponding fO_2 in felsic melt calculated from S contents in apatite, as well as the distribution of S content in zircon-hosted apatite. The relationship between S-in-apatite $S^{6+}/\Sigma S$ is calculated by the empirical formula proposed by Parat et al. (2011). The relationship between $S^{6+}/\Sigma S$ and ΔFMQ is calculated based on the work of Sun and Yao (2024).

observations from the Slave Craton (Meng et al., 2022), suggest that sulfate-containing felsic magmatism was ubiquitous in the Archean. These globally occurring oxidized magmas in the Archean are intriguing. Modern arc magmas generally have higher fO_2 than mid-ocean ridge magmas and back-arc basin magmas (Brounce et al., 2014; Kelley and Cottrell, 2009) and many arc rocks exhibit high apatite S contents (Fig. 8). The oxidized compositions of arc magmas may result from either the incorporation of oxidized crustal materials in the arc mantle sources (Brounce et al., 2014; Kelley and Cottrell, 2009; Parkinson and Arculus, 1999; Stolper et al., 2019) or intracrustal differentiation and/or assimilation processes (Lee et al., 2005; Lee et al., 2010; Tang et al., 2018; Tollan and Hermann, 2019). In the Archean, the free oxygen content in the atmosphere was less than 0.001 % of that of today (Lyons et al., 2014). The sulfate content of Archean seawater was very low (<2.5 μmol/L), and surface materials were extremely reduced (Canfield et al., 2000; Crowe et al., 2014; Holland, 2006). There are some biotic and abiotic geological records indicating the existence of local and transient oxygen accumulation events in the atmosphere during the Archean, prior to the GOE (~2.7 Ga and ~2.5 Ga, respectively) (Anbar et al., 2007; Brocks et al., 1999). Materials from these local oxidized "hotspots" might contribute to heterogeneous mantle fO_2 through plate subduction or sagduction (e.g., the high fO_2 Neoarchean subduction-metasomatized peridotites in eastern Hebei, the North China Craton reported by Wu et al. (2024)). However, the extent of mantle and crust oxidation caused by these local and transient surface oxygen accumulation processes was likely limited, thus may not explain the widely occurring sulfate-containing Archean TTG melts. Alternatively, magnetite in serpentinite may serve as an important oxidizing agent. Sulfur in fluids in equilibrium with this magnetite may become oxidized and be transferred to the mantle wedge (Beaudry and Sverjensky, 2024; Debret and Sverjensky, 2017). This oxidation mechanism remains viable even under the highly anoxic surface conditions of the Archean.

Tang et al. (2018) proposed that the fractional crystallization of garnet may cause $Fe^{3+}/\Sigma Fe$ to rise in the residual melt because the garnet crystallization and retention tend to deplete Fe^{2+} but not Fe^{3+} in the melt. Garnet is a typical high-pressure phase mineral, and crustal thickening caused by processes like orogenesis may have stabilized garnet during the formation of some Archean TTG magmas (Condie, 2014; Moyen and Martin, 2012; Moyen and Stevens, 2006; Palin et al., 2016). Therefore, garnet retention/fractionation may have been prevalent in the formation of TTGs. Considering that the crystallization of garnet can increase fO_2 by up to >2 orders of magnitude (Tang et al., 2024b), the endogenic oxidation effect associated with garnet retention/fractionation can potentially convert a significant portion of S^{2-} to S^{6+} in these TTG magmas. The impact of garnet-driven oxidation on S has been observed in the Gangdese magmatic orogen and was thought to play an important role in porphyry Cu deposit formation (Lee and Tang, 2020; Tang et al., 2020a).

Another possibility of oxidation is driven by the kinetic loss of hydrogen from hydrous melts to mantle peridotite (Tollan and Hermann, 2019). Tollan and Hermann (2019) proposed that, during the reactions between ascending hydrous magmas and the surrounding mantle, hydrogen is incorporated into mantle orthopyroxene, which promotes the dissociation of water and ultimately leads to a rise of fO_2 in the residual melt. Although such interactions in TTG formation are debated (Hawkesworth et al., 2004; Moyen and Martin, 2012; Rabinowicz et al., 2001), this oxidation is also endogenic and provides another potential oxidation mechanism that does not require external oxidized sources. According to the calculations of Tollan and Hermann (2019), dissociation of 0.2 wt% H_2O is sufficient to raise melt $Fe^{3+}/\Sigma Fe$ from

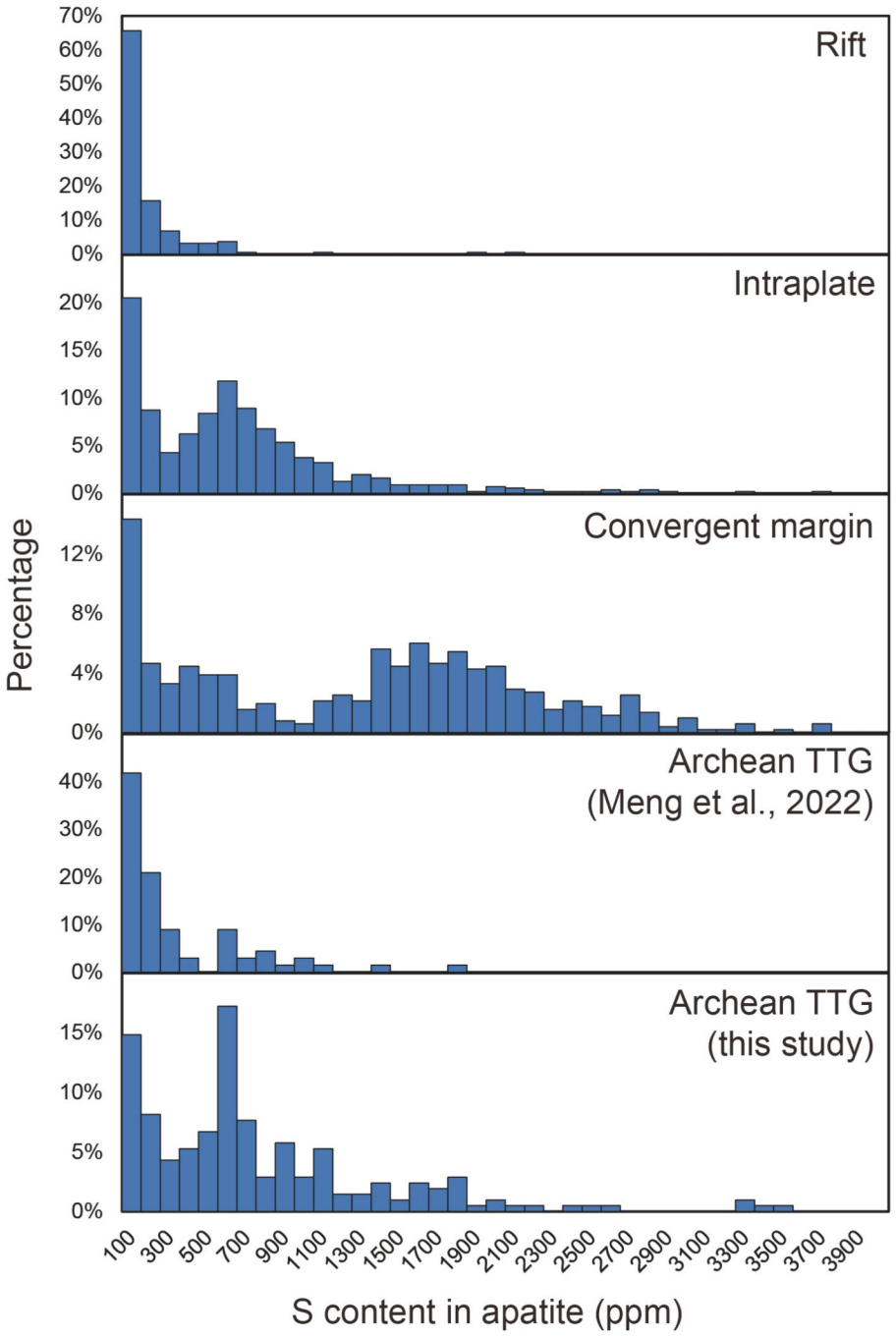


Fig. 8. Distributions of S content in apatite in felsic rocks of different tectonic settings. Intraplate and convergent margin data come from the data compiled by Li et al. (2024). Rift data come from Li et al. (2024) and Connors et al. (2020). Archean TTG data come from Meng et al. (2022) and this study.

mid-ocean ridge basalt (MORB) levels to arc basalt levels.

Our observations do not allow us to distinguish among the oxidation mechanisms mentioned above. It is possible that multiple mechanisms contributed to the oxidation of the Archean TTGs or their source rocks. The endogenic oxidation driven by garnet fractionation may have taken place at both mantle and crust levels, depending on whether the parental TTG magmas were formed by slab melting or at the base of thickened crust (Tang et al., 2018; Tang et al., 2019). By contrast, the exogenic oxidation driven by slab-derived sulfate-rich fluids and the endogenic oxidation driven by water dissociation and H loss may have primarily occurred at mantle levels (Beaudry and Sverjensky, 2024; Debret and Sverjensky, 2017; Tollan and Hermann, 2019). However, if the oxidation occurred in the mantle, one may also expect to see oxidized mafic rocks in the Archean, which appear to be rare (Aulbach and Stagno, 2016; Gao et al., 2022; Li and Lee, 2004). In addition, the lack of correlation between S content of zircon-hosted apatite inclusions and the whole-rock Ba/Th ratio (Fig. 4C) is not consistent with fluid addition during subduction or sagduction as a major source of oxidized S in TTG formation. The search for oxidized mafic rocks in the future may provide critical evidence of the oxidation mechanisms of the Archean TTGs.

One final important implication pertains to the S cycle in the Archean. In the Archean, the weathering flux of S was much lower than it is today due to reduced surface conditions, and the total S flux to continental shelves was dominated by volcanic S degassing (Stüeken et al., 2012). The flux of volcanic S degassing depends on magmatic activity and how much S is retained in the magma at the point of

degassing or fluid exsolution. Sulfur solubility in reduced felsic magmas is low, typically in the range of 50–300 ppm (Baker and Moretti, 2011; Jego and Dasgupta, 2014; Liu et al., 2007). Oxidation of S^{2-} to S^{6+} would prevent S sequestration by sulfide during magmatic differentiation and increase sulfur solubility to >1000 ppm in felsic magmas (Jugo, 2009; Keays, 1995; Moretti and Baker, 2008). As a consequence, the emergence of oxidized magmas across major Archean cratons may have not only changed the speciation of degassed S but also substantially increased the fluxes of magmatic S degassing into the Archean atmosphere. At present, reconstructing magmatic history in the Archean is challenging due to poorly preserved geologic records. Here we use the growth rates of the Archean continental crust estimated in previous studies for our calculation, which likely represent the lower limit of the actual magma flux because much of the continental crust has been destructed and recycled. Various Archean continental crust growth models indicate that the Archean continental crust increased by 10 % to 45 % of the present volume of the continental crust during the 3.5 Ga to 2.5 Ga period (Cawood et al., 2022), corresponding to the growth rate of 0.7 to 3.2 km^3/yr. For comparison, the modern volume of magmas degassed per year is approximately 2–98 km^3 based on the data from modern erupting volcanoes (Carn et al., 2017; Stoiber et al., 1987). Therefore, our estimate of the Archean felsic magma flux (0.7 to 3.2 km^3/yr) is indeed conservative and probably lower than the actual value. For those apatite grains in which S content exceeds 2000 ppm, the calculated S^{6+} content of the melt is about 100–1000 ppm. If all magmatic S were degassed, magmatic S degassing flux may reach an order of 10^{11} mol/yr or even higher in the Archean (Fig. 9). Sulfur degassing flux of this magnitude would be on the same order of magnitude as the total S flux to the continental shelves in the Archean (Stüeken et al., 2012) and play an important role in the Archean S cycle. As such, the rise of S flux to the continental shelves recorded in the Neoarchean sedimentary records may also be explained by evolving tectonism and/or magmatism. This tectonism/magmatism control is consistent with increasing melting depth of TTG source in the late Archean (Martin and Moyen, 2002), which may have resulted from either deeper subduction or more vigorous orogenesis (Tang et al., 2020b). The increased magmatic S flux may have expanded Earth's surface S reservoirs. This expansion of surface S reservoirs would enhance the role of S in modulating Earth's surface redox cycling (Canfield, 2004), which together with the rise of oxidized magmatism may have contributed to the advent of the great oxidation event at the Archean-Proterozoic boundary (Gaillard et al., 2011; Holland, 2002; Lyons et al., 2014).

6. Conclusions

We measured the S contents in separated apatite grains and zircon-hosted apatite inclusions in Archean TTG samples from the North China Craton, Kaapvaal Craton, and Pilbara Craton. The new S-in-apatite data, together with TTG whole-rock composition data, CL imaging, and EPMA mapping results, lead to several key findings:

1. Sulfur contents of separated apatite grains in Archean TTGs may have been altered by the late-stage differentiation or post-crystallization processes. These processes may include magmatic fluid exsolution, re-equilibrium with late-stage low $S^{6+}/\Sigma S$ fluids/melts, and metamorphic devolatilization, which tend to cause S loss in apatite.
2. Apatite grains encapsulated by other minerals, particularly zircon, are less affected by S loss and are more likely to retain primary magmatic S content signatures
3. Sulfate-containing and relatively oxidized (>FMQ + 1.4) magmatic systems already existed in the North China Craton, Kaapvaal Craton, and Pilbara Craton during the Archean. The oldest TTGs with these

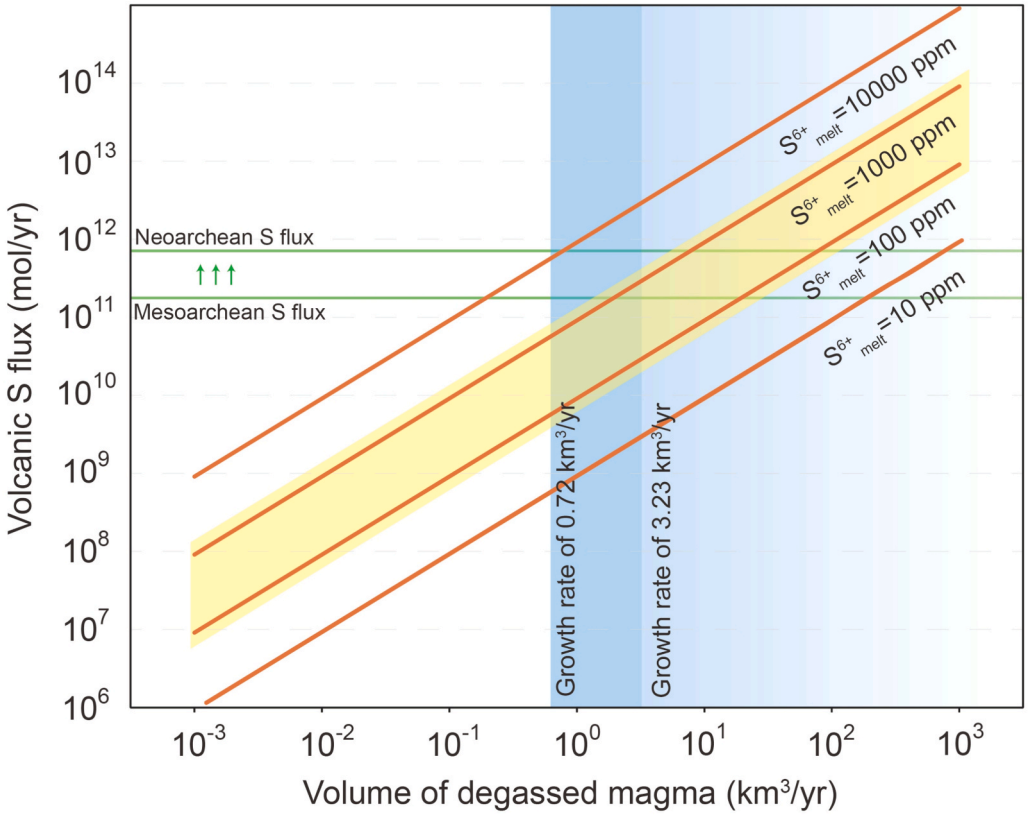


Fig. 9. The calculated Archean volcanic S flux. The deep blue bar represents the volume of magma degassed per year calculated by the growth rate of Archean continental crust. The green lines represent the total weathering S flux to continental margins during Mesoarchean and Neoarchean (Stüeken et al., 2012). The yellow bar represents the possible volcanic S flux revealed by our high S-in-apatite data.

oxidized signatures date back to 3230 Ma. These oxidized magma systems may have had a significant impact on S cycling and redox conditions of the overall anoxic surface environment in the Archean.

CRediT authorship contribution statement

Jiazhen Wang: Writing – original draft, Visualization, Investigation, Formal analysis. **Ming Tang:** Writing – review & editing, Visualization, Supervision, Project administration, Funding acquisition, Conceptualization. **Hao Chen:** Writing – review & editing, Investigation. **Xiao-Lei Wang:** Resources. **Bin Wu:** Resources, Investigation.

Declaration of competing interest

The authors declare that they have no known competing financial interests or personal relationships that could have appeared to influence the work reported in this paper.

Acknowledgements

We sincerely thank executive editor Hailiang Dong and associate editor Xiao-Ming Liu for their efficient handling. We thank Patrick Beaudry and two other anonymous reviewers for their constructive comments which significantly improved the quality of our manuscript. We thank Xuanyu Liu and Ning Ding for their contributions during the writing of the original manuscript. We thank Dongguang Yang for his assistance during the experiments of EPMA. We thank the Geological Survey of Western Australia for providing core samples from the Pilbara Craton and Mimi Chen for her assistance in the sample application. This work was financially supported by the National Key Research and Development Program of China (grant 2023YFF0803801) and the National Natural Science Foundation of China (grants 42073026 and 42125302). M. Tang is grateful for the support from the New Cornerstone Science Foundation through the XPLORER PRIZE.

Appendix A. Supplementary material

Supplementary Material to this article includes a PDF file and a spreadsheet file. The PDF file contains the detailed description of analytical methods including whole-rock major and trace element analyses, zircon U-Pb dating analysis, apatite cathodoluminescence imaging, and apatite EPMA elemental abundance analysis. The PDF file also contains supplementary figures including TTG classification, thin section photomicrographs, apatite CL images, apatite EPMA mapping results, and others. The spreadsheet file contains three tables, which include the TTG whole-rock composition information, all the EPMA data of apatite, and the zircon geochronology data, respectively. Supplementary material to this article can be found online at https://doi.org/10.1016/j.gca.2025.10.027.

Data availability

Data are available through Mendeley Data at https://doi.org/10.17632/vhcxgm5gc3.2.

References

Anbar, A.D., Duan, Y., Lyons, T.W., Arnold, G.L., Kendall, B., Creaser, R.A., Kaufman, A. J., Gordon, G.W., Scott, C., Garvin, J., Buick, R., 2007. A whiff of oxygen before the great oxidation event? Science (American Association for the Advancement of Science) 317 (5846), 1903–1906.

Anhaeusser, C.R., Robb, L.J., 1980. Regional and detailed field and geochemical studies of Archean trondhjemitic gneisses, migmatites and greenstone xenoliths in the southern part of the Barberton Mountain Land, South Africa. Precambr. Res. 11 (3–4), 373–397.

Arndt, N.T., et al., 1991. The age of the Fortescue Group, Hamersley Basin, Western Australia, from ion microprobe zircon U-Pb results. Aust. J. Earth Sci. 38 (3), 261–281.

Arth, J.G., Hanson, G.N., 1972. Quartz diorites derived by partial melting of eclogite or amphibolite at mantle depths. Contrib. Miner. Petrol. 37 (2), 161–174.

Aulbach, S., Stagno, V., 2016. Evidence for a reducing Archean ambient mantle and its effects on the carbon cycle. Geology 44 (9), 751–754.

Aulbach, S., Woodland, A.B., Stern, R.A., Vasilyev, P., Heaman, L.M., Viljoen, K.S., 2019. Evidence for a dominantly reducing Archaean ambient mantle from two redox proxies, and low oxygen fugacity of deeply subducted oceanic crust. Sci. Rep. 9 (1), 20190.

Baker, D.R., Moretti, R., 2011. Modeling the solubility of sulfur in magmas: a 50-year old geochemical challenge. Rev. Mineral. Geochem. 73 (1), 167–213.

Beaudry, P., Jagoutz, O., Bauer, A.M., Rezeau, H., Reimink, J.R., Grove, T.L., Izon, G., Ono, S., 2025. Major-element, trace-element and sulfur-isotope evidence for arc-like magmatism in the 4.0–2.9 Ga Acasta Gneiss complex. Contrib. Miner. Petrol. 180 (9).

Beaudry, P., Sverjensky, D.A., 2024. Oxidized sulfur species in slab fluids as a source of enriched sulfur isotope signatures in arcs. Geochem. Geophys. Geosyst. 25 (7).

Brocks, J.J., Logan, G.A., Buick, R., Summons, R.E., 1999. Archean molecular fossils and the early rise of eukaryotes. Science (American Association for the Advancement of Science) 285 (5430), 1033–1036.

Brounce, M.N., Kelley, K.A., Cottrell, E., 2014. Variations in $Fe^{3+}/\sum Fe$ of mariana arc basalts and mantle wedge fO_2. J. Petrol. 55 (12), 2513–2536.

Canfield, D.E., 2004. The evolution of the Earth surface sulfur reservoir. Am. J. Sci. 304 (10), 839–861.

Canfield, D.E., Habicht, K.S., Thamdrup, B., 2000. The Archean sulfur cycle and the early history of atmospheric oxygen. Science (American Association for the Advancement of Science) 288 (5466), 658–661.

Carn, S.A., Fioletov, V.E., McLinden, C.A., Li, C., Krotkov, N.A., 2017. A decade of global volcanic SO_2 emissions measured from space. Sci. Rep. 7 (1).

Cawood, P.A., Chowdhury, P., Mulder, J.A., Hawkesworth, C.J., Capitanio, F.A., Gunawardana, P.M., Nebel, O., 2022. Secular evolution of continents and the earth system. Rev. Geophys. 60 (4).

Cherniak, D.J., Watson, E.B., 2003. Diffusion in zircon. Rev. Mineral Geochem. 53 (1), 113–143.

Condie, K.C., 2014. Growth of continental crust; a balance between preservation and recycling. Mineral. Mag. 78 (3), 623–637.

Connors, L., Carley, T.L., Fiege, A., 2020. Apatite as a monitor of dynamic magmatic evolution at Torfajökull volcanic center, Iceland, dynamic magma. Evolution. 61–88.

Crowe, S.A., Paris, G., Katsev, S., Jones, C., Kim, S.-T., Zerkle, A.L., Nomosatryo, S., Fowle, D.A., Adkins, J.F., Sessions, A.L., Farquhar, J., Canfield, D.E., 2014. Sulfate was a trace constituent of Archean seawater. Science 346 (6210), 735–739.

Debret, B., Sverjensky, D.A., 2017. Highly oxidising fluids generated during serpentinite breakdown in subduction zones. Sci. Rep. 7 (1).

Evans, K.A., 2012. The redox budget of subduction zones. Earth-Sci. Rev. 113 (1–2), 11–32.

Fortin, M.-A., Riddle, J., Desjardins-Langlais, Y., Baker, D.R., 2015. The effect of water on the sulfur concentration at sulfide saturation (SCSS) in natural melts. Geochimica et Cosmochimica Acta 160, 100–116.

Gaillard, F., Scaillet, B., Arndt, N.T., 2011. Atmospheric oxygenation caused by a change in volcanic degassing pressure. Nature 478 (7368), 229–232.

Gao, L., Liu, S., Cawood, P.A., Hu, F., Wang, J., Sun, G., Hu, Y., 2022. Oxidation of Archean upper mantle caused by crustal recycling. Nat. Commun. 13 (1), 3283.

Ge, R., Zhu, W., Wilde, S.A., Wu, H., 2018. Remnants of Eoarchean continental crust derived from a subducted proto-arc. Sci. Adv. 4 (2), eaao3159.

Ge, R.F., Wilde, S.A., Zhu, W.B., Wang, X.L., 2023. Earth's early continental crust formed from wet and oxidizing arc magmas. Nature 623 (7986), 334–339.

Harlov, D.E., Casaus, J., Konecke, B.A., Simon, A.C., 2025. Experimental metasomatic incorporation of sulfur into fluorapatite as a function of coupled substitutions involving sodium, silicon, iron, and cerium. Geochimica et Cosmochimica Acta 393, 268–289.

Hastie, A.R., Fitton, J.G., Bromiley, G.D., Butler, I.B., Odling, N.W.A., 2016. The origin of Earth's first continents and the onset of plate tectonics. Geology 44 (10), 855–858.

Hawkesworth, C., George, R., Turner, S., Zellmer, G., 2004. Time scales of magmatic processes. Earth Planet. Sci. Lett. 218 (1), 1–16.

Hernández-Uribe, D., 2024. Generation of Archaean oxidizing and wet magmas from mafic crustal overthickening. Nat. Geosci. 17 (8), 809–813.

Hickman, A.H., Van Kranendonk, M.J., 2012. Early Earth evolution; evidence from the 3.5-1.8 Ga geological history of the Pilbara region of Western Australia. Episodes 35 (1), 283–297.

Holland, H.D., 2002. Volcanic gases, black smokers, and the great oxidation event. Geochimica et Cosmochimica Acta 66 (21), 3811–3826.

Holland, H.D., 2006. The oxygenation of the atmosphere and oceans. Philos. Trans. Royal Soc. B: Biol. Sci. 361 (1470), 903–915.

Hughes, J.M., Rakovan, J.F., 2015. Structurally robust, chemically diverse: apatite and apatite supergroup minerals. Elements 11 (3), 165–170.

Jagoutz, O., Schmidt, M.W., Enggist, A., Burg, J.-P., Hamid, D., Hussain, S., 2013. TTG-type plutonic rocks formed in a modern arc batholith by hydrous fractionation in the lower arc crust. Contrib. Mineral. Petrol. 166 (4), 1099–1118.

Jego, S., Dasgupta, R., 2014. The fate of sulfur during fluid-present melting of subducting basaltic crust at variable oxygen fugacity. J. Petrol. 55 (6), 1019–1050.

Johnson, T.E., Brown, M., Gardiner, N.J., Kirkland, C.L., Smithies, R.H., 2017. Earth's first stable continents did not form by subduction. Nature 543 (7644), 239–242,231–211.

Jugo, P.J., 2009. Sulfur content at sulfide saturation in oxidized magmas. Geology 37 (5), 415–418.

Keays, R.R., 1995. The role of komatiitic and picritic magmatism and S-saturation in the formation of ore deposits. Lithos 34 (1–3), 1–18.

Kelley, K.A., Cottrell, E., 2009. Water and the oxidation state of subduction zone magmas. Science (American Association for the Advancement of Science) 325 (5940), 605–607.
Konecke, B.A., Fiege, A., Simon, A.C., Holtz, F., 2017a. Cryptic metasomatism during late-stage lunar magmatism implicated by sulfur in apatite. Geology 45 (8), 739–742.
Konecke, B.A., Fiege, A., Simon, A.C., Linsler, S., Holtz, F., 2019. An experimental calibration of a sulfur-in-apatite oxybarometer for mafic systems. Geochimica et Cosmochimica Acta 265, 242–258.
Konecke, B.A., Fiege, A., Simon, A.C., Parat, F., Stechern, A., 2017b. Co-variability of S6+, S4+, and S2−in apatite as a function of oxidation state: implications for a new oxybarometer. Am. Mineral. 102 (3), 548–557.
Lee, C.-T., Leeman, W.P., Canil, D., Li, Z.-X.A., 2005. Similar V/Sc systematics in MORB and arc basalts: implications for the oxygen fugacities of their mantle source regions. J. Petrol. 46 (11), 2313–2336.
Lee, C.-T.A., Luffi, P., Le Roux, V., Dasgupta, R., Albaréde, F., Leeman, W.P., 2010. The redox state of arc mantle using Zn/Fe systematics. Nature 468 (7324), 681–685.
Lee, C.-T.A., Tang, M., 2020. How to make porphyry copper deposits. Earth Planet. Sci. Lett. 529.
Li, W.-R., Bernard, O., Utami, S.B., Phua, M., 2024. Volatile systematics in terrestrial igneous apatite: from microanalysis to decoding magmatic processes. Contrib. Mineral. Petrol. 179 (7), 76.
Li, Z.-X., Lee, C.-T., 2004. The constancy of upper mantle fO2 through time inferred from V/Sc ratios in basalts. Earth Planet. Sci. Lett. 228 (3–4), 483–493.
Liu, D.Y., Nutman, A.P., Compston, W., Wu, J.S., Shen, Q.H., 1992. Remnants of > or =3800 Ma crust in the Chinese part of the Sino-Korean Craton. Geology (Boulder) 20 (4), 339–342.
Liu, Y., Samaha, N.-T., Baker, D.R., 2007. Sulfur concentration at sulfide saturation (SCSS) in magmatic silicate melts. Geochimica et Cosmochimica Acta 71 (7), 1783–1799.
Loucks, R.R., Fiorentini, M.L., Henríquez, G.J., 2020. New Magmatic oxybarometer using trace elements in zircon. J. Petrol. 61 (3).
Lyons, T.W., Reinhard, C.T., Planavsky, N.J., 2014. The rise of oxygen in Earth's early ocean and atmosphere. Nature 506 (7488), 307–315.
Martin, H., Moyen, J.-F.O., 2002. Secular changes in tonalite-trondhjemite-granodiorite composition as markers of the progressive cooling of earth. Geology 30 (4), 319–322.
Meng, X., Richards, J.P., Kontak, D.J., Simon, A.C., Kleinsasser, J.M., Marsh, J.H., Stern, R.A., Jugo, P.J., 2021. Variable modes of formation for tonalite–trondhjemite–granodiorite–diorite (TTG)-related porphyry-type Cu ± Au deposits in the Neoarchean southern abitibi subprovince (Canada): evidence from petrochronology and oxybarometry. J. Petrol. 62 (11).
Meng, X., Simon, A.C., Kleinsasser, J.M., Mole, D.R., Kontak, D.J., Jugo, P.J., Mao, J., Richards, J.P., 2022. Formation of oxidized sulfur-rich magmas in Neoarchaean subduction zones. Nat. Geosci. 15 (12), 1064–1070.
Moreira, H., Storey, C., Bruand, E., Darling, J., Fowler, M., Cotte, M., Villalobos-Portillo, E.E., Parat, F., Seixas, L., Philippot, P., Dhuime, B., 2023. Sub-arc mantle fugacity shifted by sediment recycling across the great oxidation event. Nat. Geosci. 16 (10), 922–927.
Moretti, R., Baker, D.R., 2008. Modeling the interplay of fO2 and fS2 along the FeS-silicate melt equilibrium. Chem. Geol. 256 (3–4), 286–298.
Moyen, J.-F., 2011. The composite Archaean grey gneisses: Petrological significance, and evidence for a non-unique tectonic setting for Archaean crustal growth. Lithos 123 (1–4), 21–36.
Moyen, J.-F., Martin, H., 2012. Forty years of TTG research. Lithos 148, 312–336.
Moyen, J.-F., Stevens, G., 2006. Experimental constraints on TTG petrogenesis; implications for Archean geodynamics. Archean Geodyn. Environ. 164, 149–175.
Moyen, J.-F., Stevens, G., Kisters, A.F.M., Belcher, R.W., Lemirre, B., 2019. TTG plutons of the Barberton Granitoid-greenstone Terrain, South Africa. Earth's Oldest Rocks 615–653.
Nicklas, R.W., Puchtel, I.S., Ash, R.D., Piccoli, P.M., Hanski, E., Nisbet, E.G., Waterton, P., Pearson, D.G., Anbar, A.D., 2019. Secular mantle oxidation across the Archean-Proterozoic boundary: evidence from V partitioning in komatiites and picrites. Geochimica et Cosmochimica Acta 250, 49–75.
Palin, R.M., White, R.W., Green, E.C.R., 2016. Partial melting of metabasic rocks and the generation of tonalitic–trondhjemitic–granodioritic (TTG) crust in the Archaean: constraints from phase equilibrium modelling. Precambr. Res. 287, 73–90.
Parat, F., Holtz, F., Streck, M.J., 2011. Sulfur-bearing magmatic accessory minerals. Rev. Mineral. Geochem. 73 (1), 285–314.
Parkinson, I.J., Arculus, R.J., 1999. The redox state of subduction zones; insights from arc-peridotites. Chem. Geol. 160 (4), 409–423.
Poujol, M., Robb, L.J., Anhaeusser, C.R., Gericke, B., 2003. A review of the geochronological constraints on the evolution of the Kaapvaal Craton, South Africa. Precambr. Res. 127 (1–3), 181–213.
Prouteau, G., Scaillet, B., 2012. Experimental constraints on sulphur behaviour in subduction zones: implications for TTG and adakite production and the global sulphur cycle since the Archean. J. Petrol. 54 (1), 183–213.
Rabinowicz, M., Genthon, P., Ceuleneer, G., Hillairet, M., 2001. Compaction in a mantle mush with high melt concentrations and the generation of magma chambers. Earth Planet. Sci. Lett. 188 (3), 313–328.
Sadove, G., Konecke, B.A., Fiege, A., Simon, A.C., 2019. Structurally bound S2−, S1−, S4+, S6+ in terrestrial apatite: the redox evolution of hydrothermal fluids at the Phillips mine, New York, USA. Ore Geol. Rev. 107, 1084–1096.
Smythe, D.J., Brenan, J.M., 2016. Magmatic oxygen fugacity estimated using zircon-melt partitioning of cerium. Earth Planet. Sci. Lett. 453, 260–266.
Smythe, D.J., Wood, B.J., Kiseeva, E.S., 2017. The S content of silicate melts at sulfide saturation: New experiments and a model incorporating the effects of sulfide composition. Am. Mineral. 102 (4), 795–803.
Song, B., Nutman, A.P., Liu, D., Wu, J., 1996. 3800 to 2500 Ma crustal evolution in the Anshan area of Liaoning Province, northeastern China. Precambr. Res. 78 (1), 79–94.
Stoiber, R.E., Williams, S.N., Huebert, B., 1987. Annual contribution of sulfur dioxide to the atmosphere by volcanoes. J. Volcanol. Geotherm. Res. 33 (1–3), 1–8.
Stolper, D.A., Bucholz, C.E., Lawrence Berkeley National Laboratory, B.C.A., 2019. Neoproterozoic to early Phanerozoic rise in island arc redox state due to deep ocean oxygenation and increased marine sulfate levels. Proc Natl. Acad. Sci. - PNAS 116 (18), 8746–8755.
Stüeken, E.E., Catling, D.C., Buick, R., 2012. Contributions to late Archaean sulphur cycling by life on land. Nat. Geosci. 5 (10), 722–725.
Sun, C., Yao, L., 2024. Redox equilibria of iron in low- to high-silica melts: a simple model and its applications to C-H-O-S degassing. Earth Planet. Sci. Lett. 638.
Tang, M., Chen, H., Song, S., Sun, G., Wang, C., 2024a. Zircon Eu/Eu* in Archean TTGs with implications for the role of endogenic oxidation in Archean crustal differentiation. Geochimica et Cosmochimica Acta 378, 259–269.
Tang, M., Erdman, M., Eldridge, G., Lee, C.T.A., 2018. The redox "filter" beneath magmatic orogens and the formation of continental crust. Sci. Adv. 4 (5), eaar4444.
Tang, M., Lee, C.-T.A., Costin, G., Höfer, H.E., 2019. Recycling reduced iron at the base of magmatic orogens. Earth Planet. Sci. Lett. 528.
Tang, M., Lee, C.-T.A., Ji, W.-Q., Wang, R., Costin, G., 2020a. Crustal thickening and endogenic oxidation of magmatic sulfur. Sci. Adv. 6 (31), eaba6342.
Tang, M., Lee, C.-T.A., Rudnick, R.L., Condie, K.C., 2020b. Rapid mantle convection drove massive crustal thickening in the late Archean. Geochimica et Cosmochimica Acta 278, 6–15.
Tang, M., Wang, J., Lee, C.-T.A., 2024b. Reevaluating the oxidation effect of garnet crystallization. Lithos 470–471.
Tollan, P., Hermann, J., 2019. Arc magmas oxidized by water dissociation and hydrogen incorporation in orthopyroxene. Nat. Geosci. 12 (8), 667–671.
Tomkins, A.G., Rebryna, K.C., Weinberg, R.F., Schaefer, B.F., 2012. Magmatic sulfide formation by reduction of oxidized arc basalt. J. Petrol. 53 (8), 1537–1567.
Van Kranendonk, M.J., Hickman, A.H., Smithies, R.H., Nelson, D.R., 2002. Geology and tectonic evolution of the Archean North Pilbara Terrain, Pilbara Craton, Western Australia. Econ. Geol. Bull. Soc. Econ. Geol. 97 (4), 695–732.
Wan, Y., Dong, C., Xie, H., Wilde, S.A., Liu, S., Li, P., Ma, M., Li, Y., Wang, Y., Wang, K., Liu, D., 2023. Hadean to early Mesoarchean rocks and zircons in the North China Craton: a review. Earth-Sci. Rev. 243.
Wang, X., Tang, M., Moyen, J., Wang, D., Kröner, A., Hawkesworth, C., Xia, X., Xie, H., Anhaeusser, C., Hofmann, A., Li, J., Li, L., 2022. The onset of deep recycling of supracrustal materials at the Paleo-Mesoarchean boundary. Natl. Sci. Rev. 9 (3).
Wilke, M., Jugo, P.J., Klimm, K., Susini, J., Botcharnikov, R., Kohn, S.C., Janousch, M., 2008. The origin of S4+ detected in silicate glasses by XANES. Am. Mineral. 93 (1), 235–240.
Wu, Z., Wang, C., Allen, M.B., Tang, M., Chen, Y., Jia, L., Song, S., 2024. Rise of mantle oxidation by Neoarchean subduction in the North China Craton. Earth Planet. Sci. Lett. 646.
Xing, C.-M., Wang, C.Y., 2017. Cathodoluminescence images and trace element compositions of fluorapatite from the Hongge layered intrusion in SW China: a record of prolonged crystallization and overprinted fluid metasomatism. Am. Mineral. 102 (7), 1390–1401.
Zhao, G., Sun, M., Wilde, S.A., Sanzhong, L., 2005. Late Archean to Paleoproterozoic evolution of the North China Craton: key issues revisited. Precambr. Res. 136 (2), 177–202.
Zhao, G., Zhai, M., 2013. Lithotectonic elements of Precambrian basement in the North China Craton: review and tectonic implications. Gondwana Res. 23 (4), 1207–1240.